

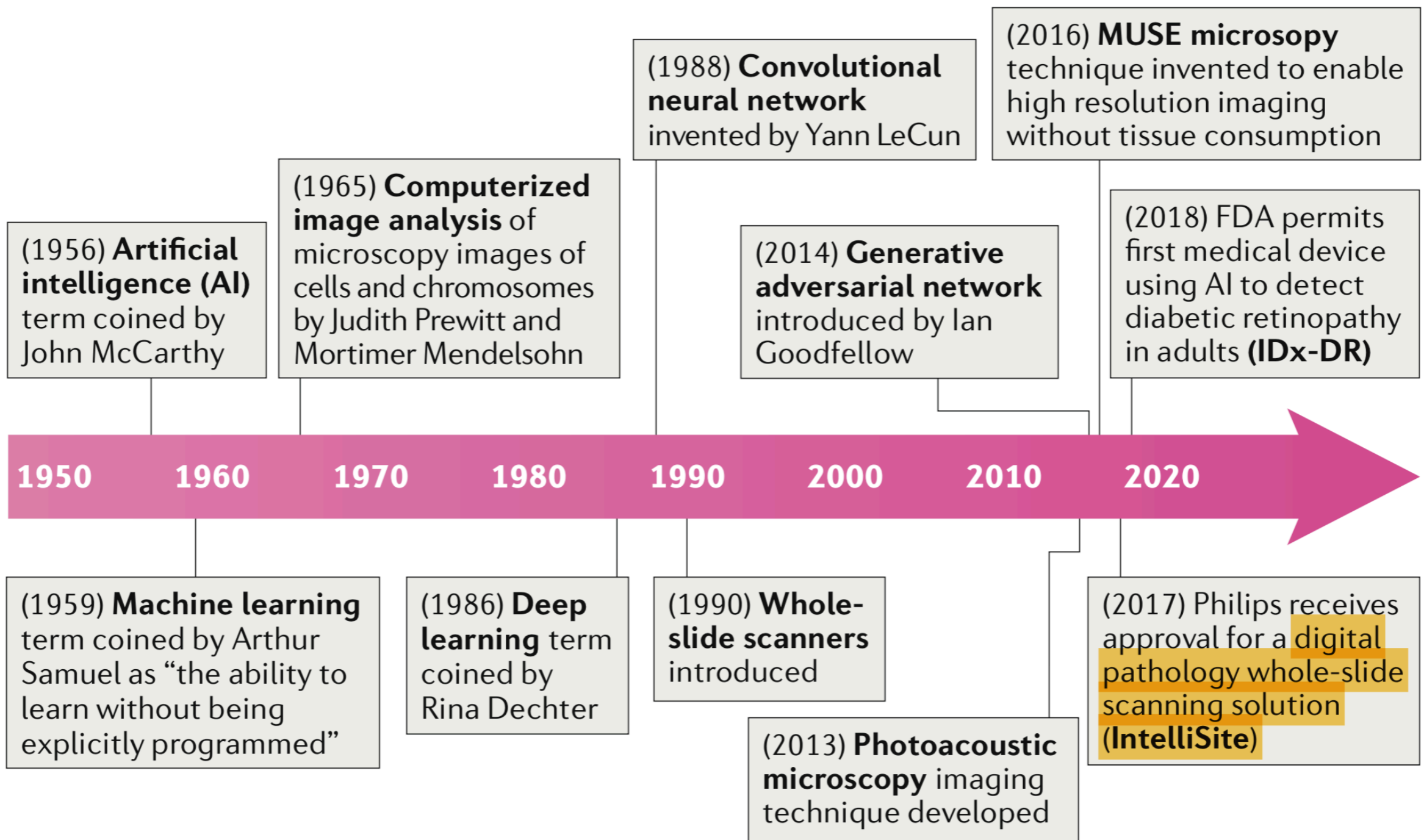
**Цифровая патология:  
примеры применения  
искусственных нейронных сетей  
в работе патоморфологов**

**Лаборатория биоинформатики  
НМИЦ АГП им. В.И. Кулакова  
Наумов В.А.  
Балашов И.С.**

## Digital pathology

Digital pathology includes the process of digitizing histopathology slides using whole-slide scanners as well as the analysis of these digitized whole-slide images (WSI) using computational approaches. Such

for precision oncology. Pathologists and oncologists are the primary end users of these image analysis approaches.



Most commonly, the result of this process is a histopathological diagnosis that is delivered in a written report to the treating physicians. While the systematic training

histopathology analysis is inherently limited by its subjective nature and the

widespread use of non-invasive or minimally invasive procedures to acquire diagnostic samples has considerably reduced the size and quality of specimens obtained, making the work of pathologists more challenging.



# Два подхода к анализу

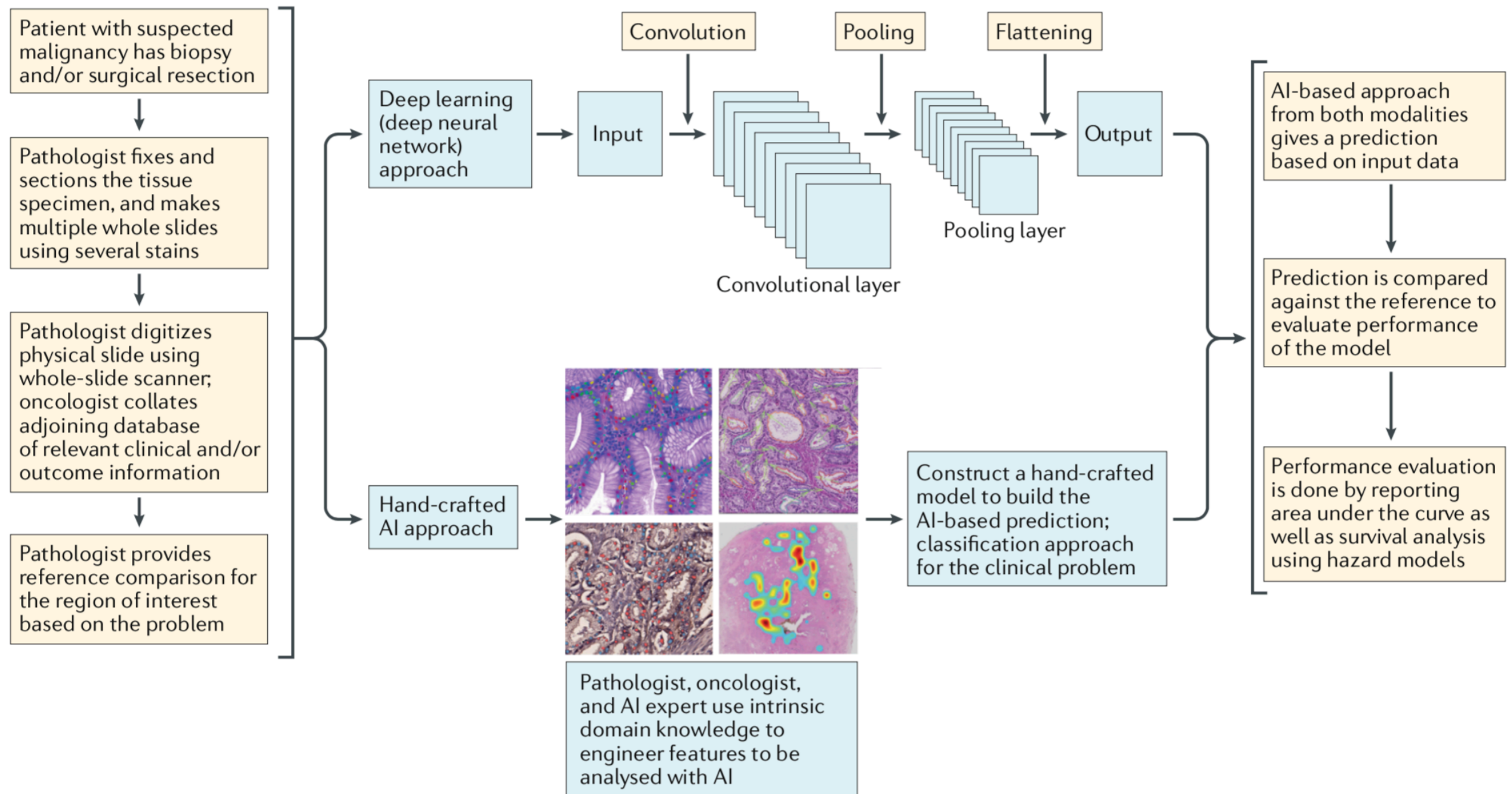


Fig. 2 | **Workflow and general framework for artificial intelligence (AI) approaches in digital pathology.** Typical steps involved in the use of two popular categories of AI approaches: deep learning and hand-crafted feature engineering.



## Два подхода к анализу

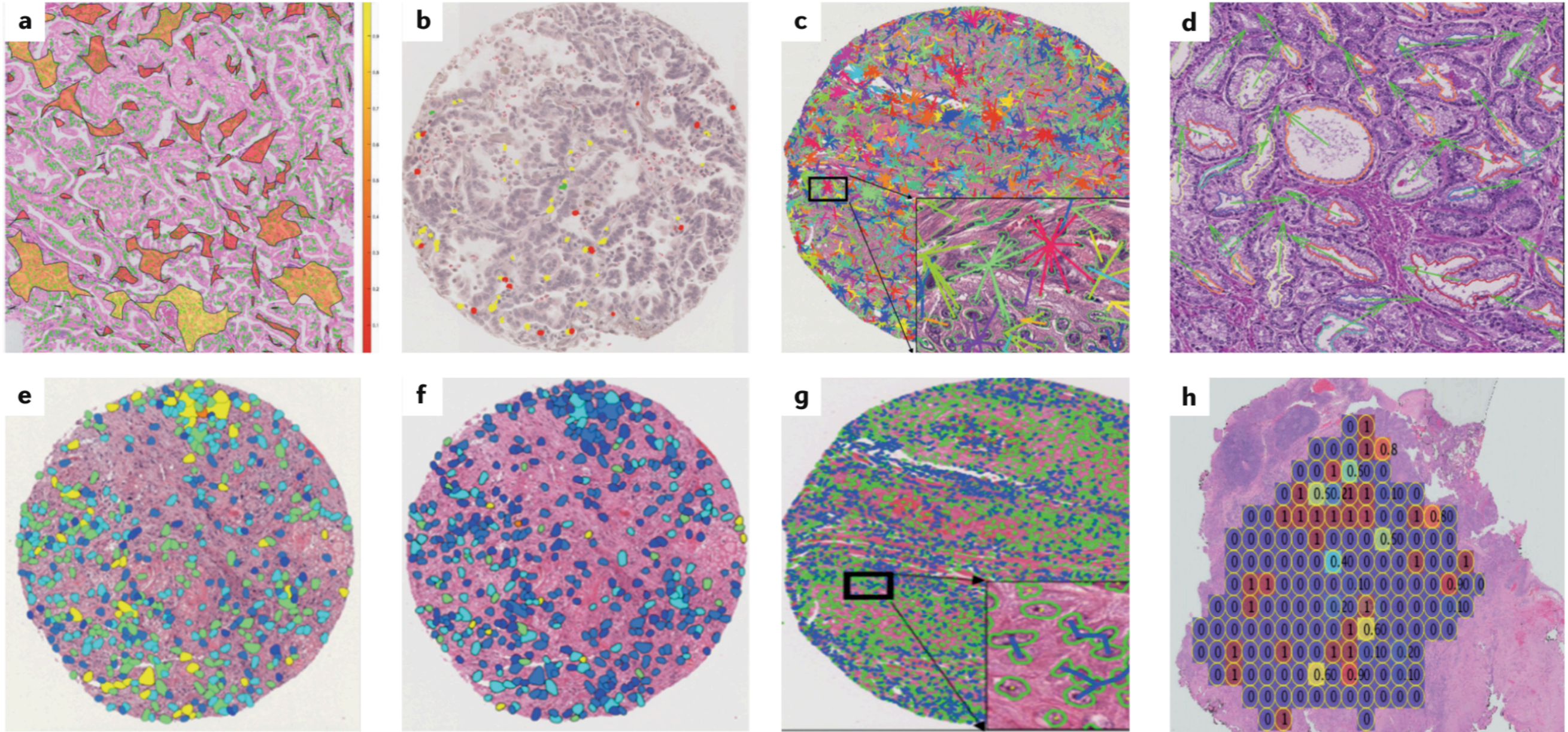


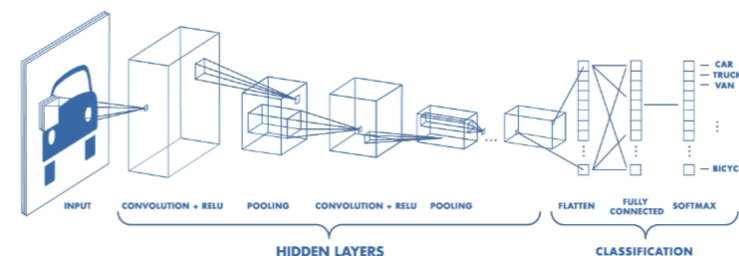
Fig. 3 | **Visual representations of hand-crafted features across cancer types.** **a** | Spatial arrangement of clusters of tissue-infiltrating lymphocytes in a non-small-cell lung carcinoma (NSCLC) whole-slide image. **b** | Features developed using quantitative immunofluorescence of tissue-infiltrating lymphocyte subpopulations (including detection of CD4<sup>+</sup> and CD8<sup>+</sup> T cells and CD20<sup>+</sup> B cells) in NSCLC samples. **c** | Features reflecting the distribution and entropy of global cell cluster graphs constructed using NSCLC specimens.

**d** | Features computing the relative orientation of the glands present in prostate cancer tissue. **e** | Diversity of texture of cancer cell nuclei in an oral cavity squamous cell carcinoma. **f** | Nuclear shape feature computed on cancer cell nuclei in a human papillomavirus-positive oropharyngeal carcinoma. **g** | Graph feature showing the spatial relationships of different cancer cell nuclei in an oral cavity carcinoma. **h** | Hand-crafted feature capturing cellular heterogeneity in an oestrogen receptor-positive breast cancer.

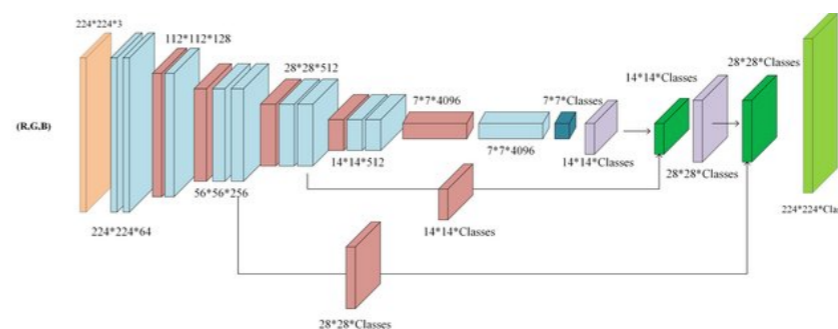


# Искусственные нейронные сети

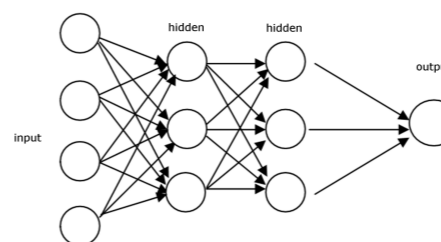
Convolutional neural networks



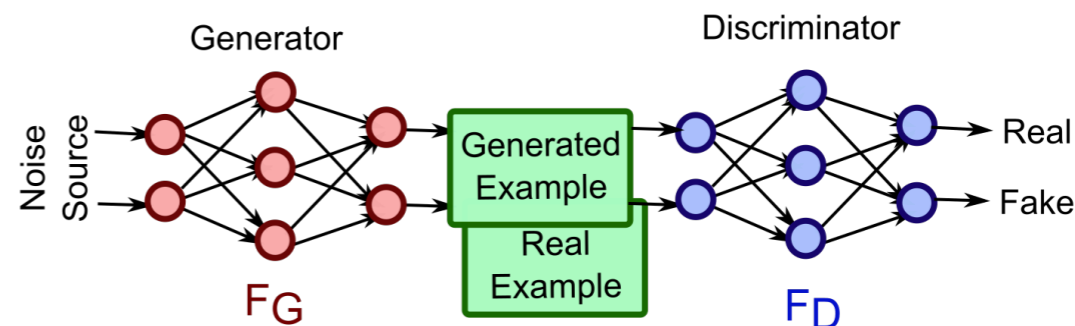
Fully convolutional networks



Recurrent neural networks



Generative adversarial networks

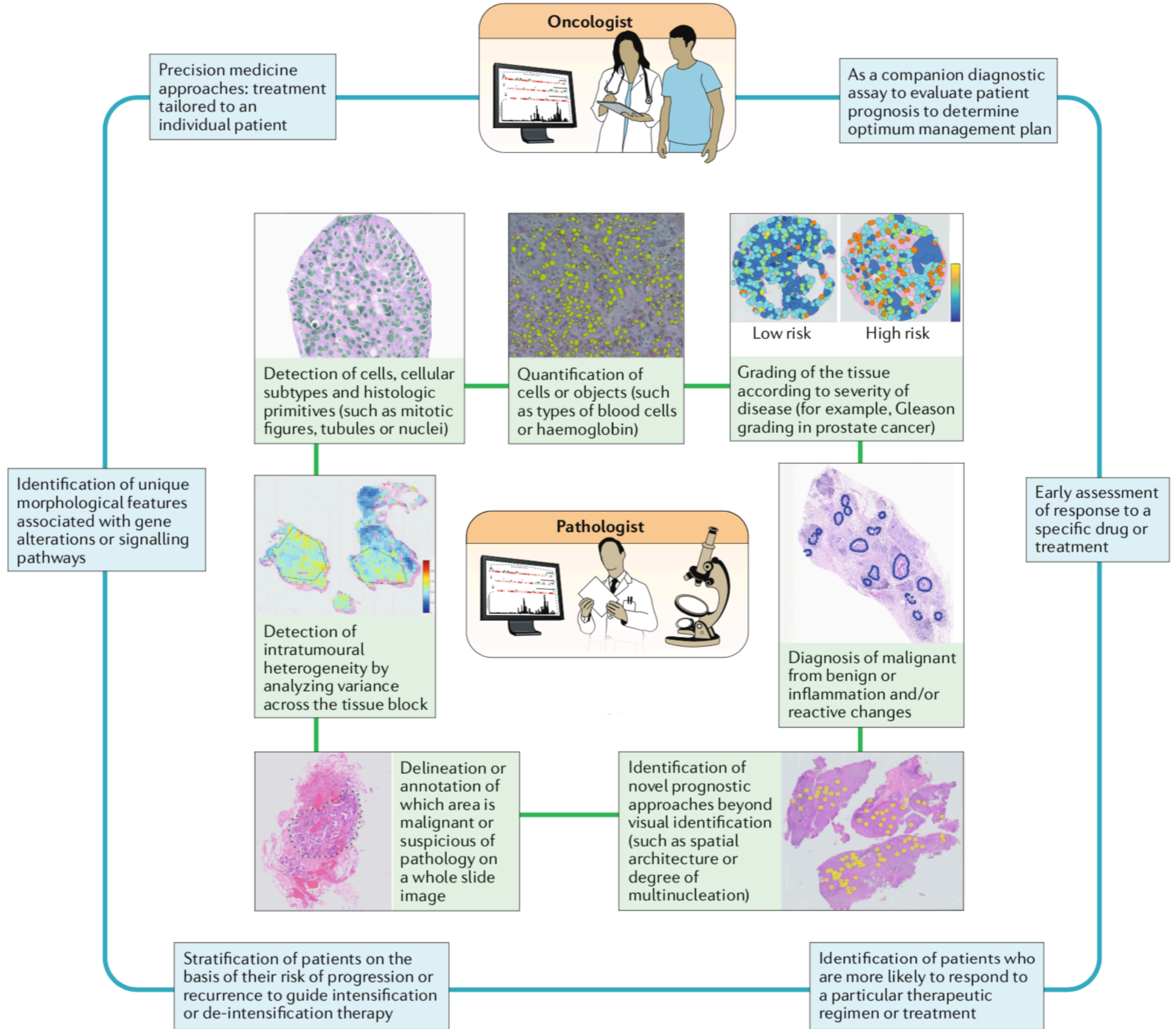


# Что можно предсказывать?

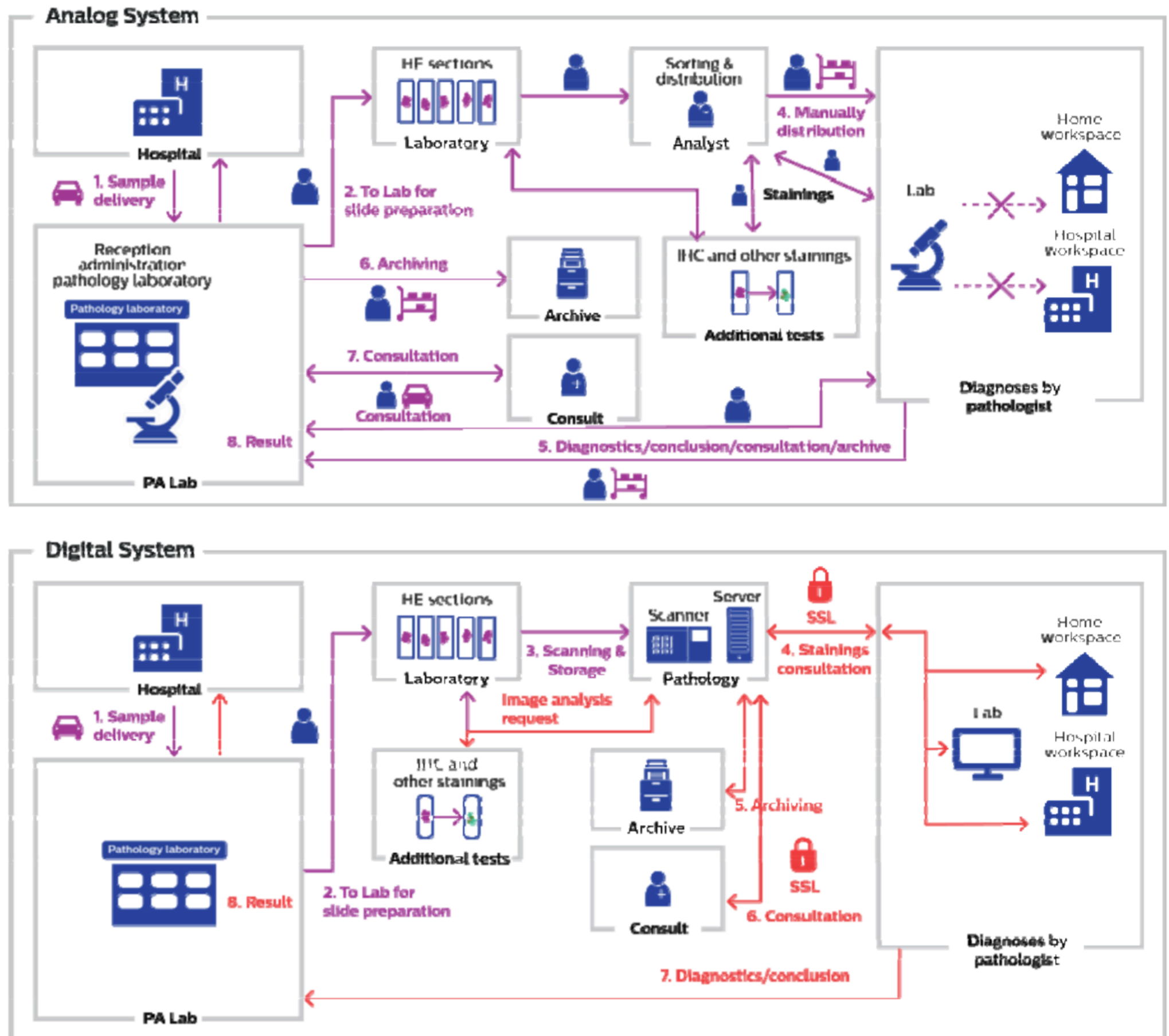
- Диагностика
- Прогноз
- Выбор терапии



# Что можно предсказывать?

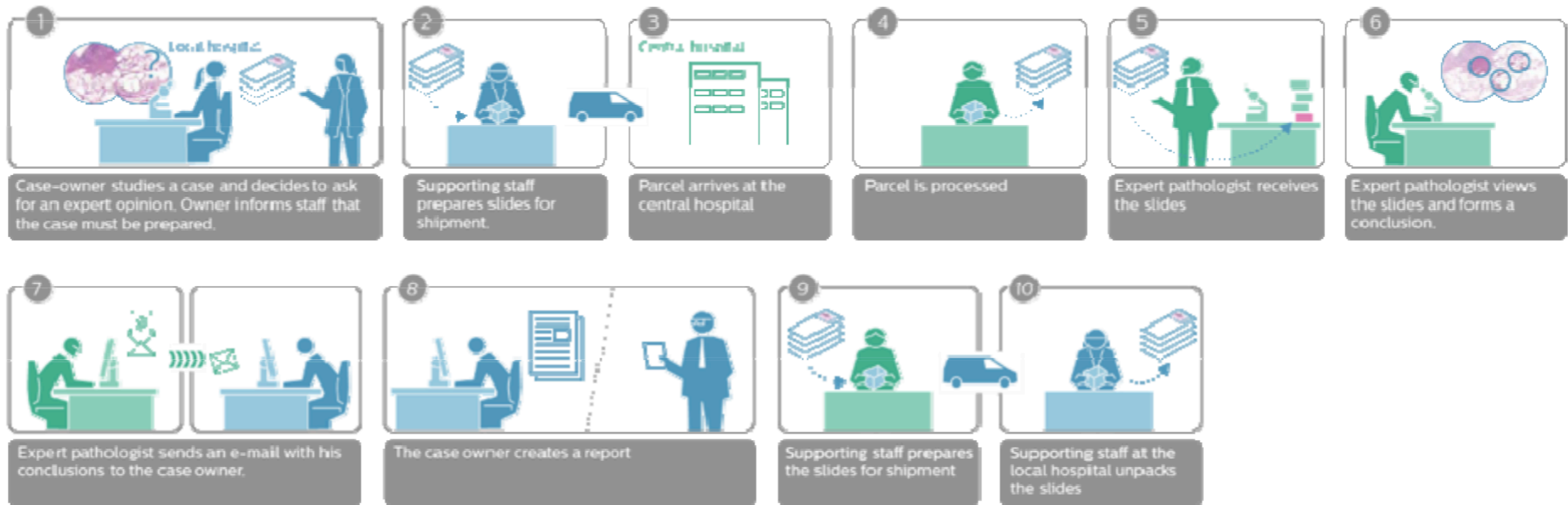


# Сравнение процессов цифровой и аналоговой патологии

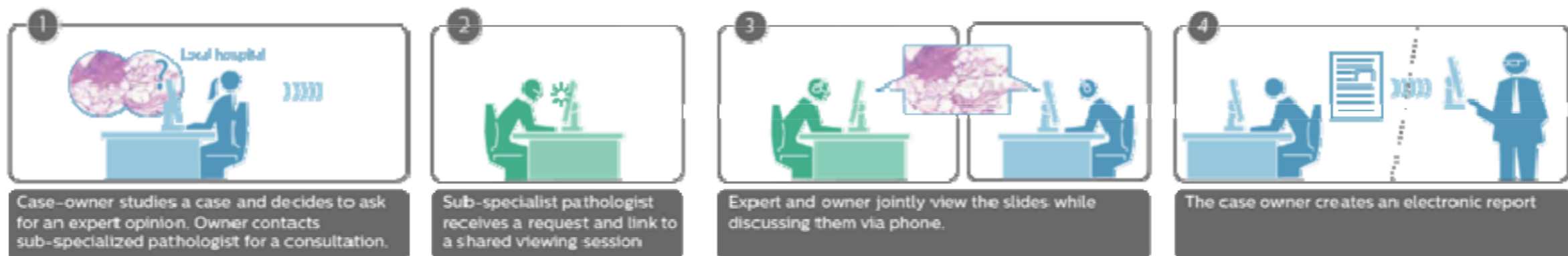


# Сравнение процессов цифровой и аналоговой патологии

## Analog workflow



## Digital workflow



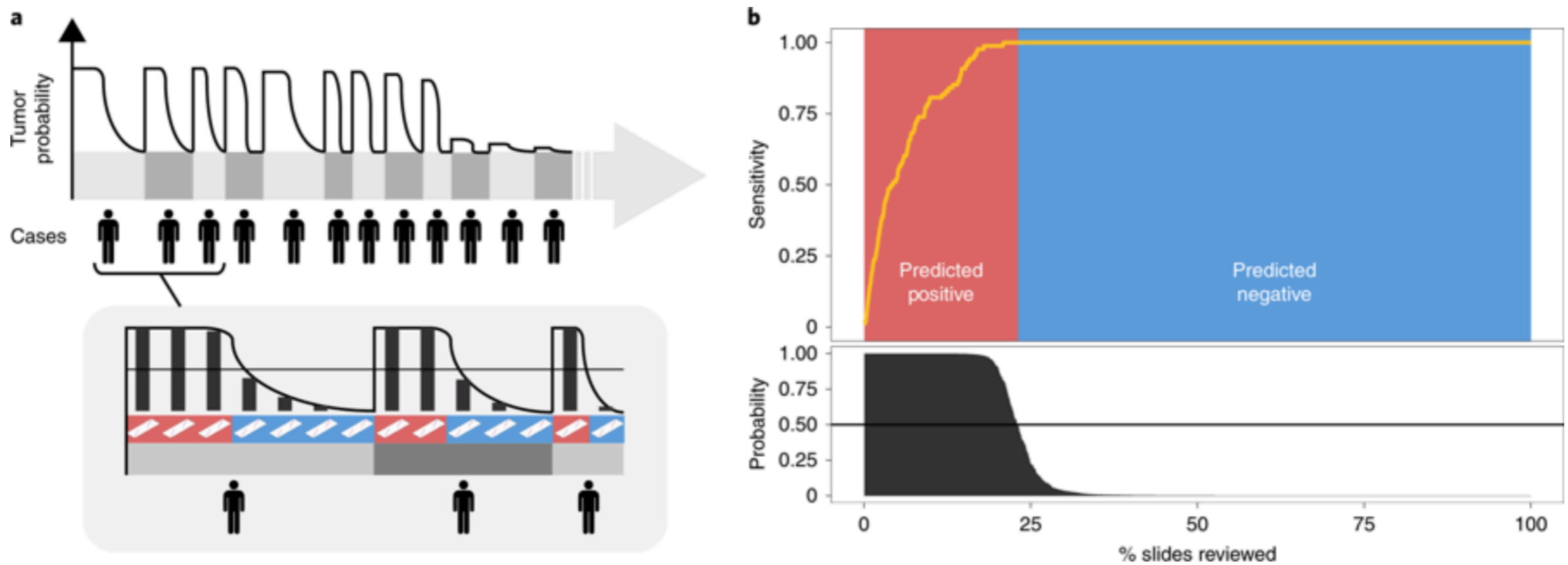
# Сравнение процессов цифровой и аналоговой патологии

**Figure 1.** *Digital pathology suite. Whole slide scanners and computers are arranged ergonomically for digital pathology supervisors and technicians to manage scanning workflow.*



# Fig. 6: Impact of the proposed decision support system on clinical practice.

From: [Clinical-grade computational pathology using weakly supervised deep learning on whole slide images](#)

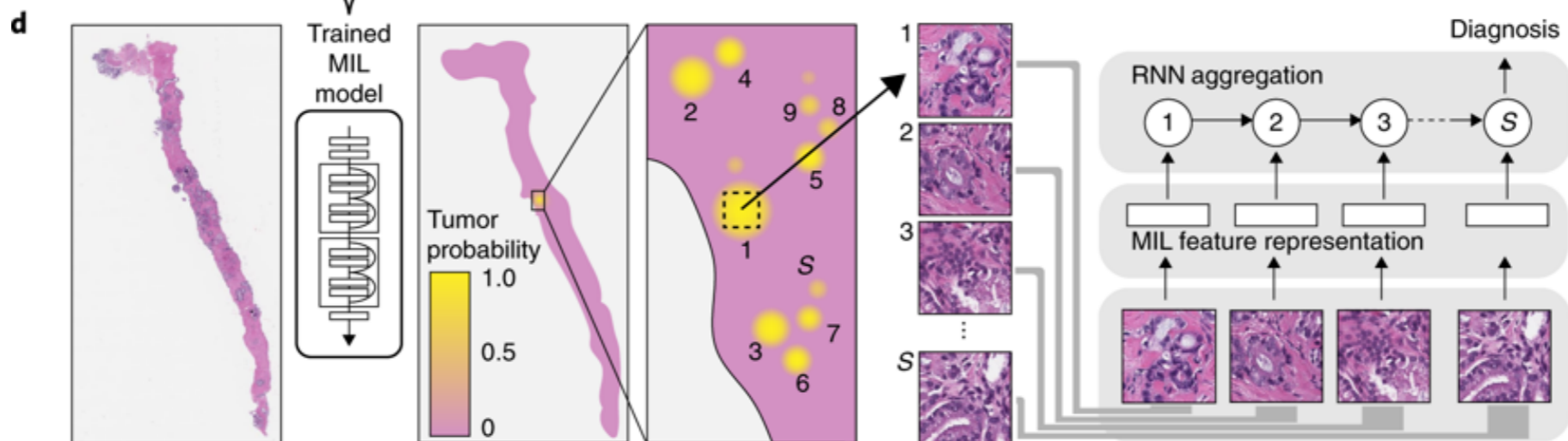
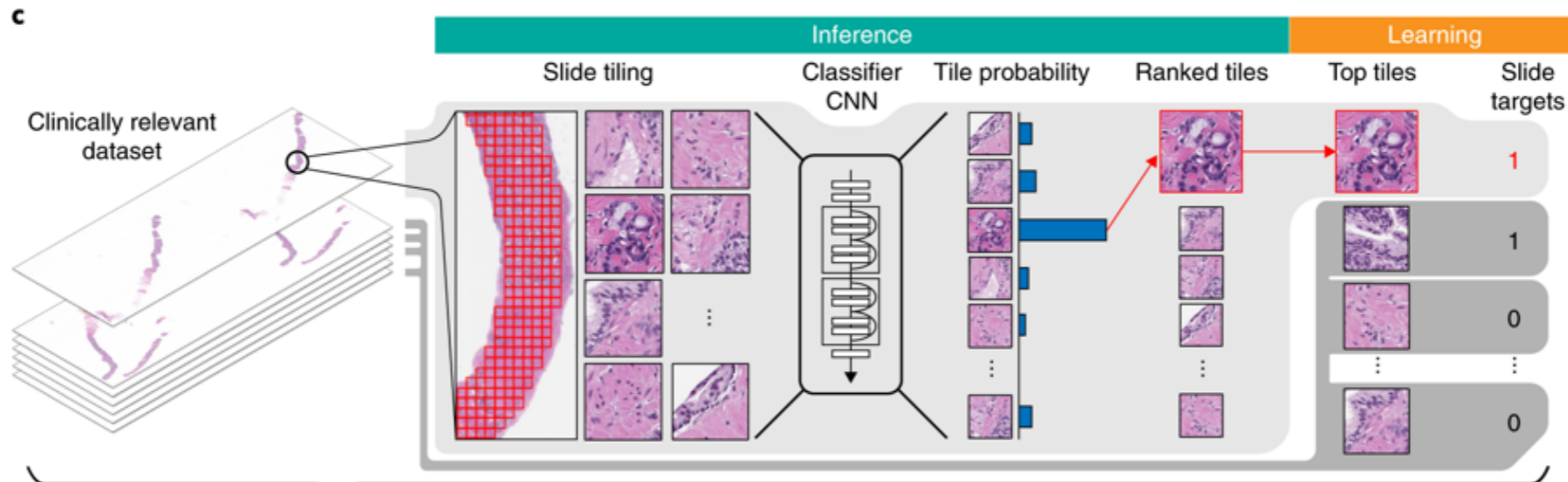
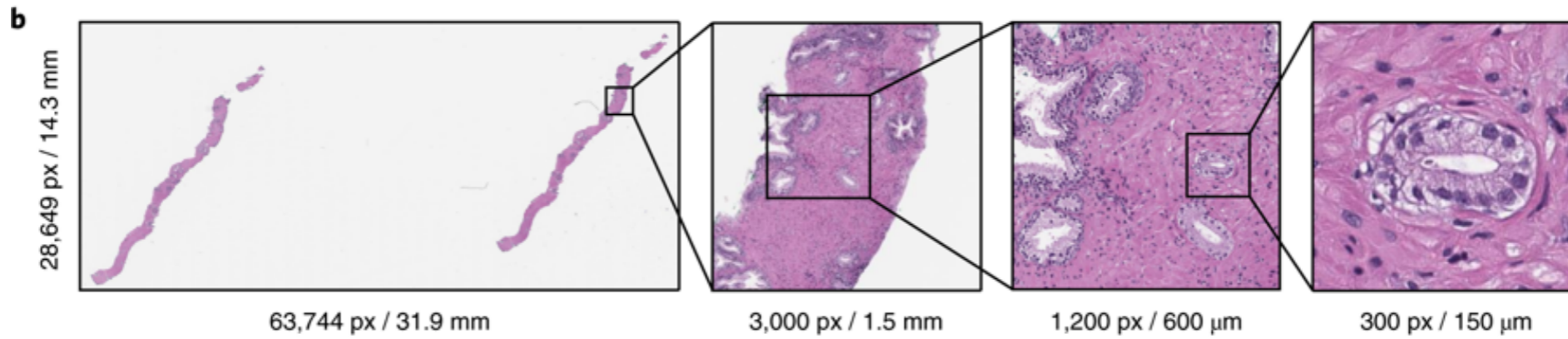


**a**, By ordering the cases, and slides within each case, based on their tumor probability, pathologists can focus their attention on slides that are probably positive for cancer. **b**, Following the algorithm's prediction would allow pathologists to potentially ignore more than 75% of the slides while retaining 100% sensitivity for prostate cancer at the case level ( $n = 1,784$ ).

<https://www.nature.com/articles/s41591-019-0508-1/figures/6>

**a**

Dataset	Years	Slides	Patients	Positive slides	External slides	ImageNet
Prostate in house	2016	12,132	836	2,402	0	19.8x
Prostate external	2015–2017	12,727	6,323	12,413	12,727	29.0x
Skin	2016–2017	9,962	5,325	1,659	3,710	21.4x
Axillary lymph nodes	2013–2018	9,894	2,703	2,521	1,224	18.2x
Total		44,732	15,187			88.4x



# Разбор одной из работ

nature  
medicine

Brief Communication | Published: 03 June 2019

## Deep learning can predict microsatellite instability directly from histology in gastrointestinal cancer

Jakob Nikolas Kather , Alexander T. Pearson, Niels Halama, Dirk Jäger, Jeremias Krause, Sven H. Loosen, Alexander Marx, Peter Boor, Frank Tacke, Ulf Peter Neumann, Heike I. Grabsch, Takaki Yoshikawa, Hermann Brenner, Jenny Chang-Claude, Michael Hoffmeister, Christian Trautwein & Tom Luedde 

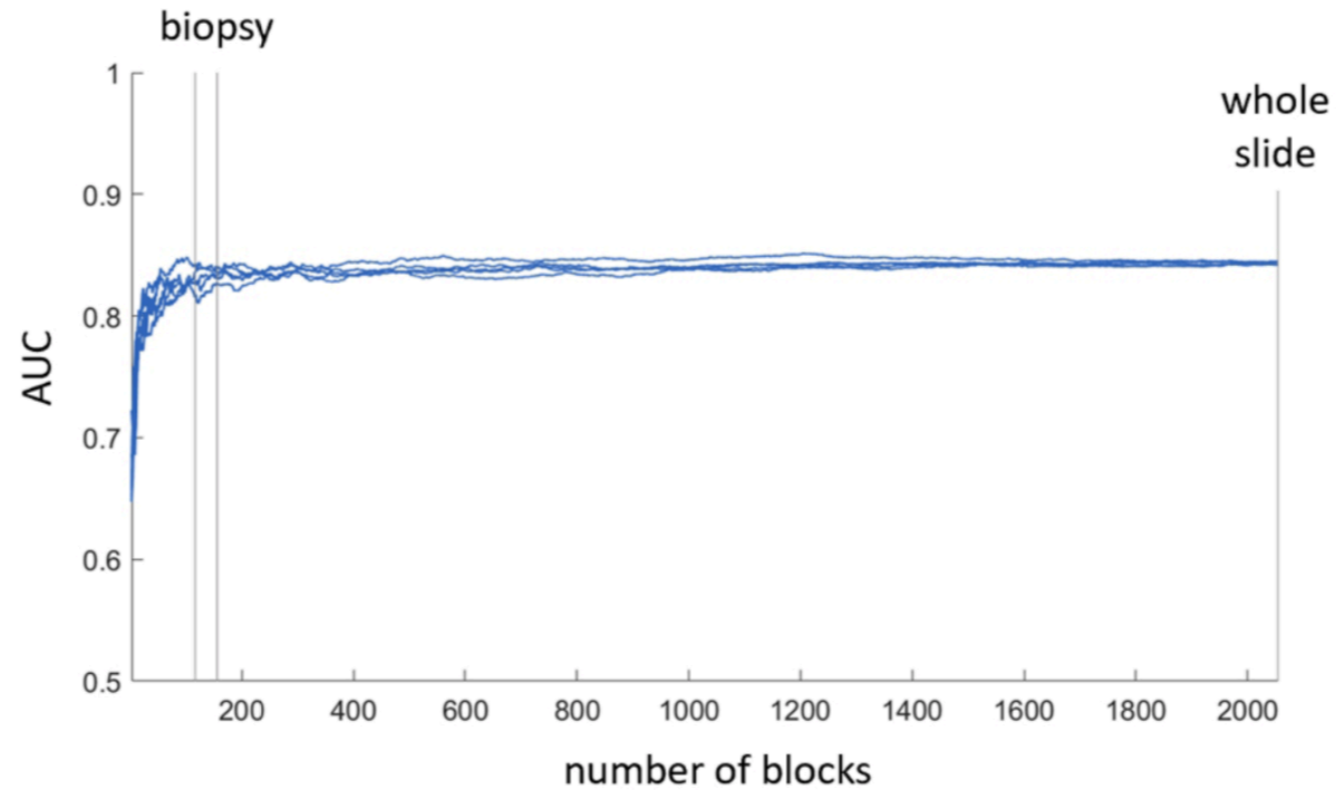
Статья о том что нейронная сеть смогла предсказать один из параметров опухоли желудка (микросателитная нестабильность) - опираясь только на микроскопические изображения. Обычно тот тест - дорогостоящая процедура, важная для диагностики, но назначаемая не всем из-за стоимости и сложности. Анализ изображений позволяет сделать этот тест всем, у кого берётся биопсия

	TCGA-STAD	TCGA-CRC-KR	TCGA-CRC-DX	TCGA-UCEC	DACHS	KCCH
Material	FFPE	snap frozen	FFPE	FFPE	FFPE	FFPE
Staining	HE	HE	HE	HE	HE	HE
N patients	315	387	360	327	378	185
Median age [years]	67	67	67	63	68	65
% UICC stage 1	13%	17%	17%	69%	20%	0%
% UICC stage 2	31%	37%	37%	6 %	33%	39%
% UICC stage 3	44%	29%	30%	19%	33%	55%
% UICC stage 4	10%	12%	13%	4%	14%	6%

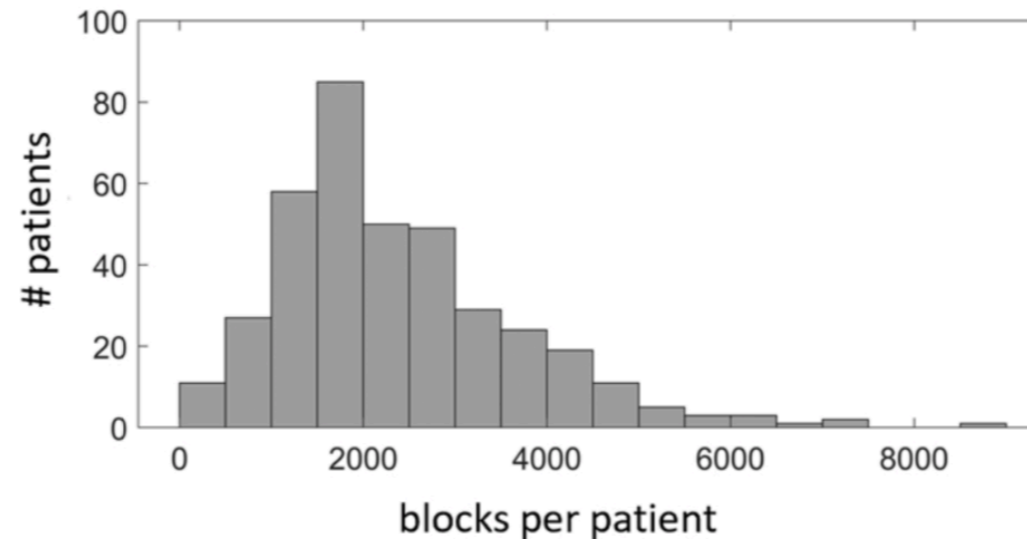
**Supplementary Table 1: Clinico-pathological variables of all patient cohorts.** STAD = stomach adenocarcinoma, CRC = colorectal cancer, KR = snap-frozen slides, DX = diagnostic slides with FFPE processing, FFPE = formalin-fixed and paraffin-embedded, HE = hematoxylin and eosin, UICC = Union internationale contre le cancer, UCEC = uterine corpus endometrial carcinoma, KCCH = Yokohama gastric cancer cohort, DACHS = German colorectal cancer cohort, MSI = microsatellite instable, NA = not applicable.



**b**



**c**



(licensed under a CC-BY 4.0 license). **b**, Classification performance in virtual biopsies. We predicted MSI status in all patients in the DACHS cohort, varying the number of blocks (tiles) from 3 to 2,054, which was the median number of blocks per whole-slide image. This experiment was repeated five times with different randomly picked blocks being used. As one block has an edge length of  $256\ \mu\text{m}$ , a 1-cm tissue cylinder with 100% tumor tissue from a standard 18G biopsy needle corresponds to 117 blocks and a 16G needle corresponds to 156 blocks. In clinical routine, usually only a part of each biopsy core contains tumor, but multiple biopsy cores are collected. With increasing tissue size, performance stabilizes at  $\text{AUC} = 0.84$ . This shows that a typical biopsy would be sufficient for MSI prediction. CI, confidence interval. **c**, Distribution of the numbers of blocks for all patients in DACHS ( $n = 378$  patients).

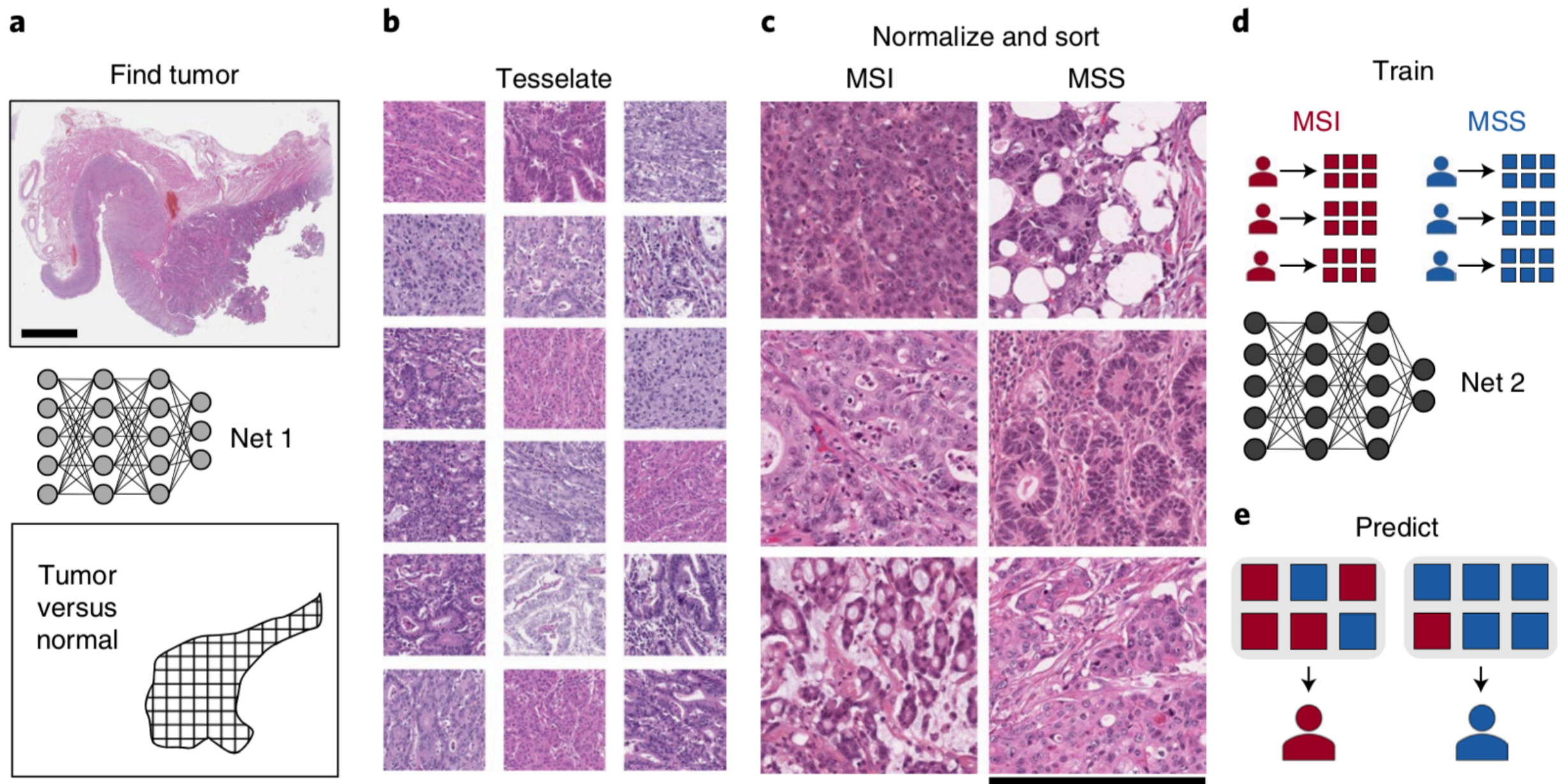


**Fig. 1 | Tumor detection and MSI prediction in H&E histology.** **a**, A convolutional neural network was trained as a tumor detector for STAD and CRC. Scale bar, 4 mm. **b,c**, Tumor regions were cut into square tiles (**b**), which were color-normalized and sorted into MSI and MSS (**c**). Scale bar, 256  $\mu$ m. **d**, Another network was trained to classify MSI versus MSS. **e**, This automatic pipeline was applied to held-out patient sets.

# Разбор одной из работ

# Результаты предсказания

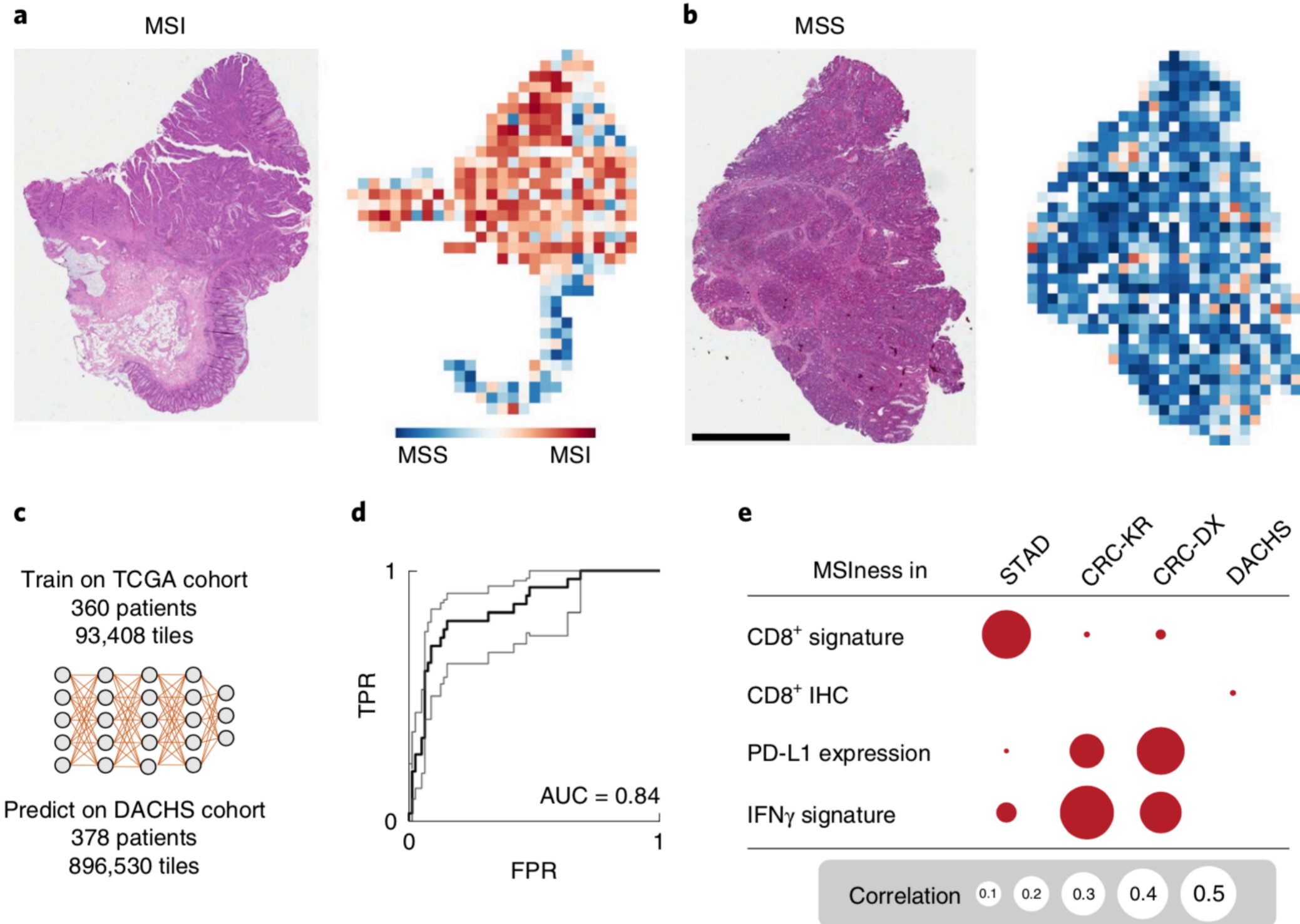
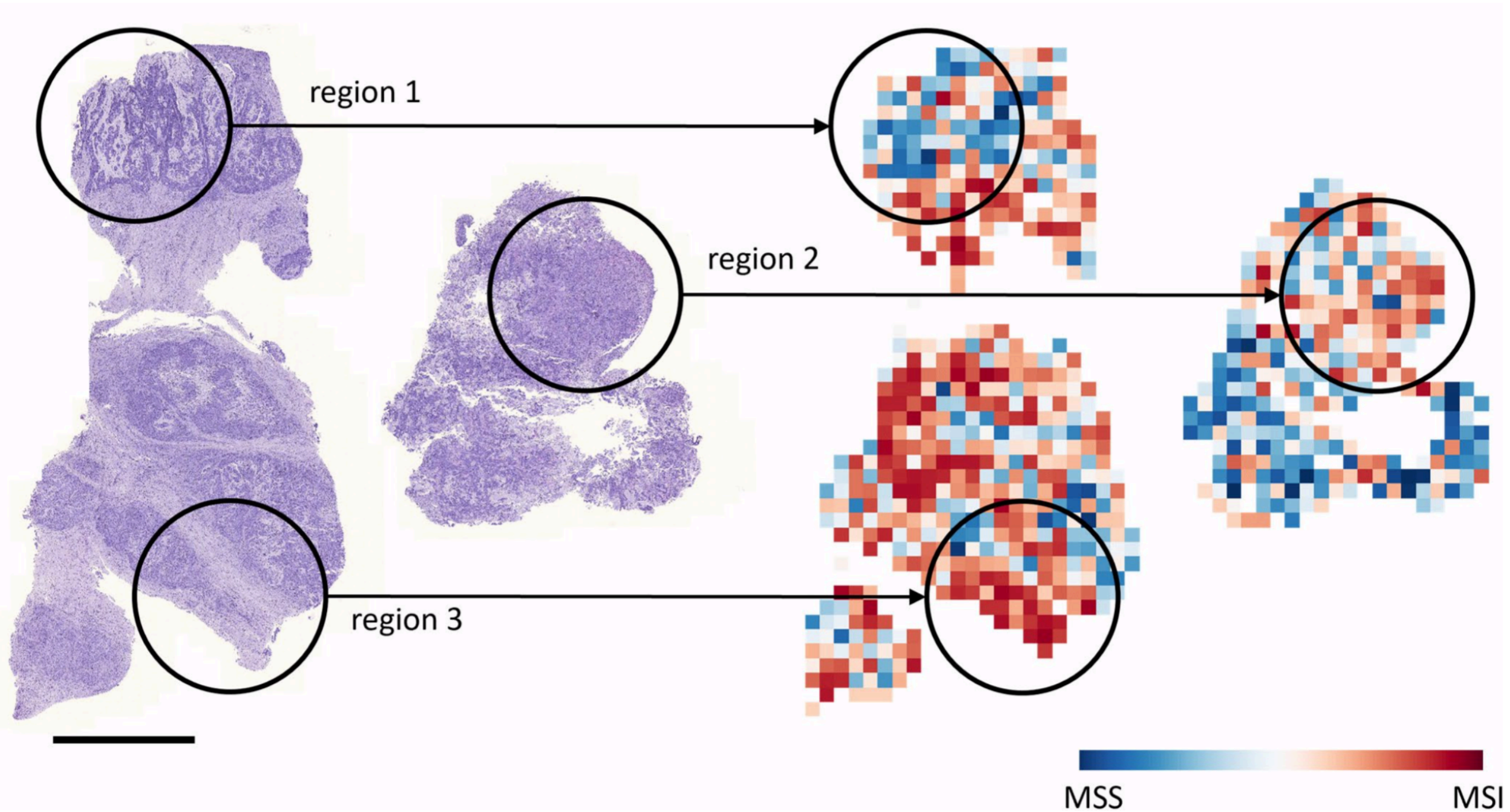


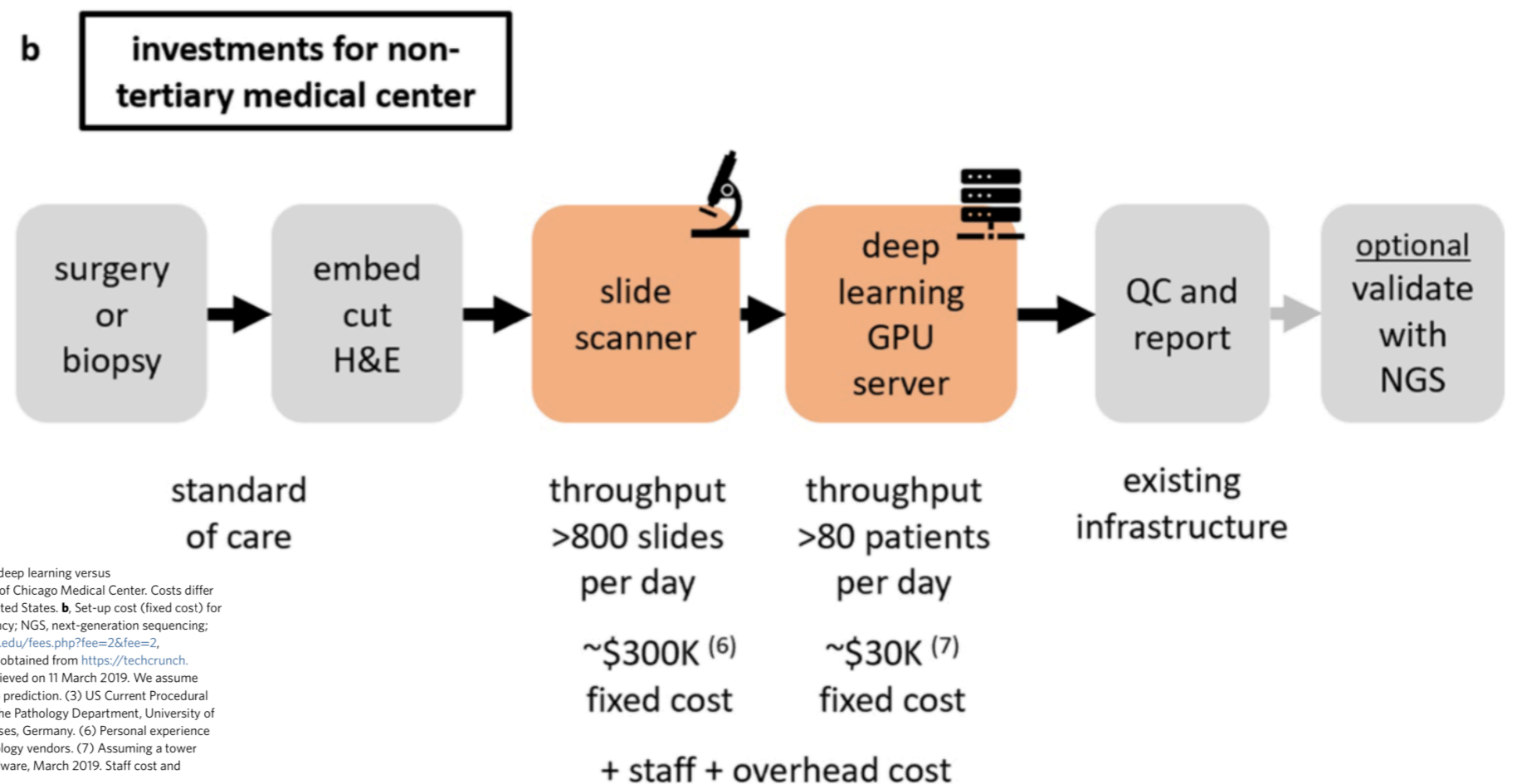
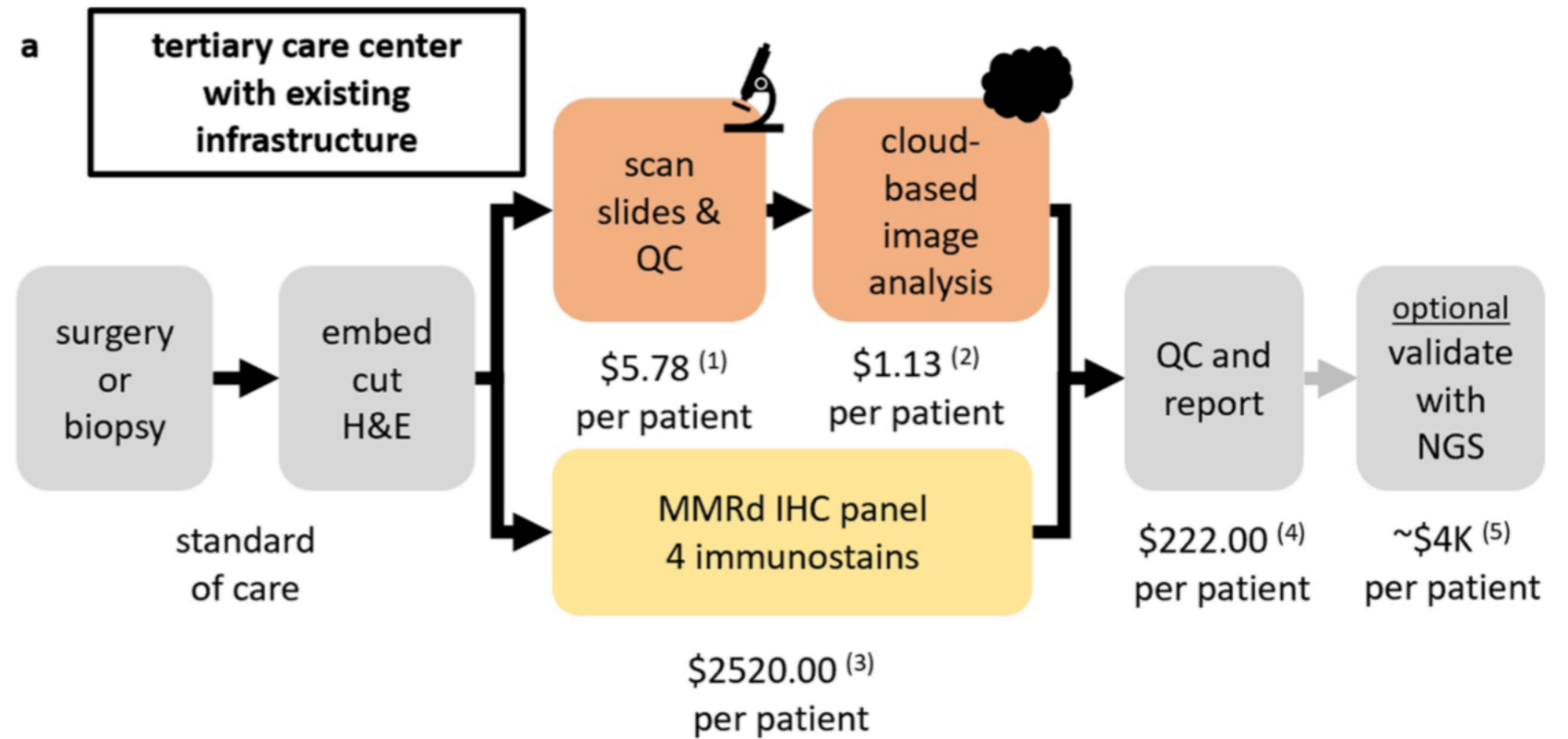
**Fig. 2 | Classification performance in an external validation set.** **a,b**, Tissue slides of patients with MSI and MSS tumors in the TCGA-CRC-DX test set show the spatial patterns of predicted MSI score (Extended Data Fig. 4). These images are representative of  $n=378$  patients. **c**, A network was trained on the TCGA-CRC-DX training cohort ( $n=260$  patients) and deployed on the DACHS cohort ( $n=378$  patients). **d**, Patient-level receiver operating characteristic curve with bootstrapped 95% CI in DACHS ( $n=378$  patients). FPR, false-positive rate ( $1 - \text{specificity}$ ); TPR, true-positive rate (sensitivity). **e**, Pearson correlation of predicted MSI to transcriptomic and immunohistochemical (IHC) data across test sets.  $P$  values are listed in Supplementary Table 4. Sample sizes per cohort are: TCGA-STAD  $n=91$ , TCGA-CRC-KR  $n=105$ , TCGA-CRC-DX  $n=95$ , DACHS  $n=134$  patients. No adjustments for multiple comparisons were made, and all statistical tests were two-sided.



**Extended Data Fig. 3 | Morphological correlates of intratumor heterogeneity of MSI.** **a**, Histological image of a test set patient who was genetically determined as MSI. **b**, Corresponding predicted MSI map for the image shown in **a**. Three regions are highlighted. Region 1 is a glandular region with necrosis and extracellular mucus; this region was predominantly predicted to be MSS. Region 2 is a solid, dedifferentiated region, which was predicted to be MSI. Region 3 contained mostly budding tumor cells mixed with immune cells, this region was strongly predicted to be MSI. Together, these representative examples show that different morphologies elicit different predictions and that these predictions can be traced back to patterns that are understandable for humans. Scale bar, 2.5 mm. This figure is representative of  $n = 378$  patients in the DACHS cohort.

# Разбор одной из работ

# Экономика



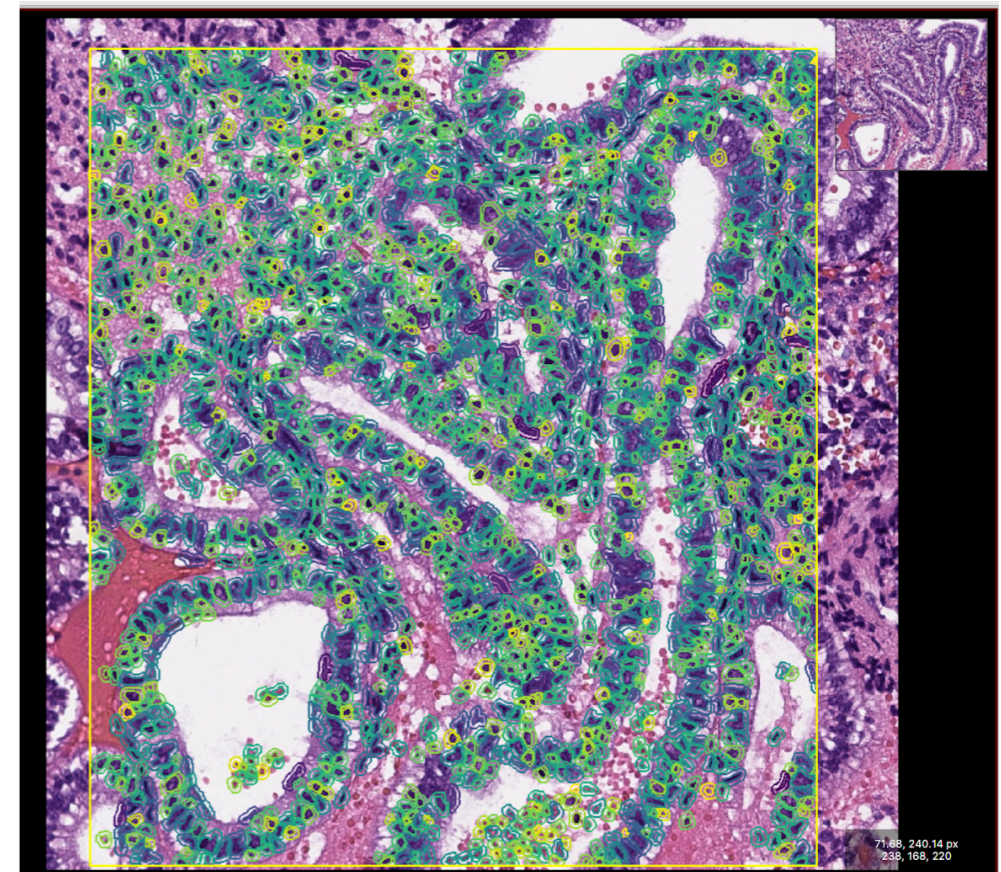
**Extended Data Fig. 4 | Estimated cost for MSI screening with deep learning.** **a.** Workflow for MSI screening with deep learning versus immunohistochemistry in tertiary care centers with existing digital pathology core facilities such as the University of Chicago Medical Center. Costs differ by country and are usually cheaper in Europe than in the United States. Here, we list the costs that apply in the United States. **b.** Set-up cost (fixed cost) for a digital pathology and deep learning infrastructure. H&E, hematoxylin and eosin; MMRd, mismatch repair deficiency; NGS, next-generation sequencing; QC, quality control. Sources and assumptions were as follows. (1) Prices were obtained from <https://htrc.uchicago.edu/fees.php?fee=2&fee=2>, retrieved on 11 March 2019. We assume x20 magnification on a high-volume whole-slide scanner. (2) Prices were obtained from <https://techcrunch.com/2019/03/07/scaleway-releases-cloud-gpu-instances-for-e1-per-hour/> and <https://www.scaleway.com/>, retrieved on 11 March 2019. We assume that 1h of GPU computing on a Nvidia Tesla P100 GPU is required to process whole-slide images for one patient to prediction. (3) US Current Procedural Terminology (CPT) code 88342, four-antibody panel at US\$852.00 per staining. (4) Personal communication by the Pathology Department, University of Chicago Medicine, March 2019. (5) Personal communication, Medical Oncology, National Center for Tumor Diseases, Germany. (6) Personal experience of cost for a high-throughput slide scanner plus a limited storing capacity, based on offers by multiple digital pathology vendors. (7) Assuming a tower server with one NVidia Tesla V100 GPU or similar GPU, based on multiple offers by providers for professional hardware, March 2019. Staff cost and infrastructure cost are not accounted for in this schematic.

# Наш опыт

Разделение на 4 компоненты (клеточных типа) на трёх стадиях методом NMF

Этапы работы с гистологическими срезами:

- автоматическая сегментация изображений на отдельные клетки
- кластеризация клеток на основе внешнего сходства
- присвоение кластерам наименований
- подсчёт соотношений различных кластеров и использование полученных соотношений в качестве весов для метода NMF



**Спасибо за внимание!**